JVST A
Journal of Vacuum Science & Technology A

Plasma polymerization of cyclopropylamine in a low-pressure cylindrical magnetron reactor: A PIC-MC study of the roles of ions and radicals

Cite as: J. Vac. Sci. Technol. A **38**, 033003 (2020); https://doi.org/10.1116/1.5142913
Submitted: 18 December 2019 . Accepted: 02 March 2020 . Published Online: 01 April 2020

Stella Mathioudaki, Cédric R. Vandenabeele, Romain Tonneau, Andreas Pflug, Jonathan Tennyson, and Stéphane Lucas

View Online
Export Citation
CrossMark

© 2020 Author(s).

ARTICLE
avs.scitation.org/journal/jva

Plasma polymerization of cyclopropylamine in a low-pressure cylindrical magnetron reactor: A PIC-MC study of the roles of ions and radicals

Cite as: J. Vac. Sci. Technol. A 38, 033003 (2020); doi: 10.1116/1.5142913
Submitted: 18 December 2019 · Accepted: 2 March 2020 ·
Published Online: 1 April 2020

View Online

Export Citation

CrossMark

Stella Mathioudaki,[1] Cédric R. Vandenabeele,[1] Romain Tonneau,[1] Andreas Pflug,[2] Jonathan Tennyson,[3] and Stéphane Lucas[1,a)]

AFFILIATIONS

[1]Laboratory of Analysis by Nuclear Reaction, Namur Institute of Structured Matter, University of Namur, Rue de Bruxelles 61, 5000 Namur, Belgium
[2]Fraunhofer Institute for Surface Engineering and Thin Films IST, Bienroder Weg 54e, 38108 Braunschweig, Germany
[3]Department of Physics and Astronomy, University College London, Gower Street, London WC1E 6BT, United Kingdom

[a)]**Author to whom correspondence should be addressed:** stephane.lucas@unamur.be

ABSTRACT

A study of plasma polymerization of cyclopropylamine in a low-pressure cylindrical magnetron reactor is presented. Both experimental and numerical approaches are used to investigate thin film growth mechanisms and polymer film properties depending on the magnetic field strength. Combining both approaches enables the consistency of the numerical model to be checked while acquiring data for understanding the observed phenomena. Samples are first analyzed by x-ray photoelectron spectroscopy, time of flight secondary ion mass spectrometry, and ion beam analysis to illustrate the differences in degrees of chemical functionalization and cross-linking between the regions of high and low magnetic fields. 3D particle-in-cell Monte Carlo collision simulations are then performed to shed light on experimental results, after implementing a set of electron-cyclopropylamine collision cross sections computed using the R-matrix method. The simulations enable the main radicals produced in the discharge to be tracked by determining their production rates, how they diffuse in the plasma, and how they absorb on the reactor walls. Additionally, the cyclopropylamine ion ($C_3H_7N^+$) behavior is followed to bring insights into the respective roles of ions and radicals during the plasma polymerization process.

Published under license by AVS. https://doi.org/10.1116/1.5142913

I. INTRODUCTION

During the last few years, amine-rich surfaces have gained increasing interest for a number of applications, including wastewater purification membranes,[1] cell colonization,[2] or biomolecule immobilization.[3] A convenient way to prepare such surfaces is to deposit a thin organic layer by plasma polymerization, which enables the surface properties to be tuned with a high level of control by a judicious choice of the precursor molecule and plasma parameters.[4] Synthesis of amine-based plasma polymer films (PPFs) is mainly focused on two features that usually follow opposite trends: the incorporation of a high content of primary amine groups (NH_2) and obtaining a stable coating in aqueous solvents.[5,6] Optimizing PPF properties is based on a good knowledge of thin film growth mechanisms.

Plasma polymerization relies on the activation of a precursor molecule in the plasma phase through collisional processes with energetic electrons and subsequent condensation of activated species on a surface.[4,7] In low pressure plasmas, electrons are characterized by an electron energy distribution function, whose most probable value is centered around 1–2 eV.[8–10] Thus, most of the electrons have an energy closer to dissociation energies of organic bonds (2–5 eV) than to ionization energies (>10 eV). This, in combination with the longer residual time of radicals, implies that the concentration of radicals in an organic discharge can be 10^3–10^5 times higher than the concentration of positive ions.[11] For this reason, it was historically assumed that the growth of a PPF in plasma deposition processes is mainly governed by radical-surface interactions, as summarized in the "rapid step growth polymerization" mechanism by Yasuda.[12]

Published under license by AVS.

Initially, ions were mainly supposed to induce chemical bond breaking after impacting the growing film surface, leading to the creation of preferential adsorption sites for reactive species and unsaturated molecules and promoting the PPF cross-linking. This phenomenon, described in the "ion-activated growth model" by d'Agostino,[13] still implies that the ion density in the plasma is too low to contribute significantly to the mass deposited. However, more recent studies brought experimental evidence that ions can play an important role in the deposition mechanisms and even be the main species responsible for PPF growth.[14,15]

Different reasons are given to explain this observation. First, ions are accelerated in the sheath that naturally develops around any floating surface immersed in a plasma, which considerably reduces to 10^2–10^3 the neutral/ion flux ratio directed toward the surface (flux being defined by density times velocity).[16] Second, due to this acceleration, ions arrive at the surface at much higher energy (15–20 eV for a floating surface) than neutrals (including radicals and intact precursor molecules, 0.03–0.05 eV), which confers to ions a much richer chemistry and generally higher sticking probabilities (0.2–1) compared with neutrals (10^{-4}–1).[7,17] Let us note that ions can have an even greater energy if the surface is polarized with a high negative voltage. Third, experimental studies have revealed the formation in the gas phase of heavy ionic oligomers of the form $(n\mathrm{M} + \mathrm{H})^+$ (with M being the precursor molecule and n an integer as high as 3–4),[18,19] which can be incorporated in the PPF and contribute to the deposited mass.[16]

Michelmore *et al.* showed that the PPF deposition mechanisms, and ultimately the final layer properties, mainly depend on the monomer structure and the power injected into the discharge. Indeed, plasma polymerization from saturated monomers is dominated by ionic deposition, while deposition from unsaturated monomers at low power is dominated by grafting of neutral species on surface dangling bonds generated by ion impacts.[20] Increasing the power delivered to unsaturated monomer discharges increases the contribution of ionic deposition due to the fragmentation of multiple bond moieties and higher ion/neutral flux ratio. These authors showed that films grown predominantly from neutral deposition (i.e., unsaturated monomer at low power) are generally denser but less cross-linked and more soluble. Nevertheless, as shown by Hegemann *et al.* in the case of ethylene-based coatings, PPF density increases with ion energy beyond a certain threshold due to hydrogen abstraction that occurs and leads to more cross-linked and harder coatings.[21]

To summarize, even if the importance of ions in the PPF growth mechanisms has been clearly demonstrated, the relative contributions of ions and radicals are still debated today. Up to now, these contributions have mainly been investigated by experimental techniques such as ion probes and mass spectrometry.[7] In the present work, we study with a numerical tool the respective roles of ions and radicals in a plasma polymerization process performed in a particular reactor geometry. The reactor is a homemade cylindrical magnetron reactor that was designed for the surface modification of powders and has already been used for the functionalization of carbon nanotubes[22] and metal oxide nanoparticles.[23] The precursor chosen is cyclopropylamine (CPA, C_3H_7N), which is a nontoxic isomer of the highly studied allylamine molecule and has recently shown a great potential to deposit stable PPFs with a high content of primary amine groups.[24–33]

Plasma modeling is extensively used to help understand plasma processes, to predict final coatings properties, to optimize plasma chambers, and to ease the scaling-up of a process.[34,35] Nevertheless, plasma simulations of organic discharges are limited to molecules with a low number of atoms and only include simple reactions due to the lack of cross sections and rate coefficients.[36] The most studied molecule is acetylene (C_2H_2) that has been investigated alone[37–40] or in combination with Ar,[41] Ar and H_2,[42] and NH_3.[17] Other molecular systems studied by plasma simulation include CF_4,[43,44] CF_4/O_2,[45] CH_4,[46] CH_4/O_2,[47] CH_4/C_2H_2,[17] or C_4F_8.[48] To date, no plasma modeling study of the CPA molecule has yet been reported.

Depending on their conditions, plasmas can be modeled using either fluid dynamics or kinetic approaches.[49,50] In fluid dynamics, equations of continuity, drift, diffusion, and energy flux are solved self-consistently with a reduced Maxwell equation for the electric potential. It is necessary to use certain assumptions for the energy distribution functions of the involved species. In the discharge geometry investigated here, a substantial part of plasma reactions and nanoparticle surface treatment is expected to happen within the plasma sheath, and, therefore, no equilibrium assumption of the local velocity distribution would hold. A proper description of this zone requires to apply kinetic methods such as the particle-in-cell Monte Carlo (PIC-MC) method, which statistically solves the Boltzman equation including the collision term.[51] Its most crucial numerical constraint is the spatial resolution of electric potential fluctuations; for numerical stability, an upper limit of the cell size proportional to the Debye length is required.[52] This considerably limits the maximum plasma density, which can be modeled with feasible effort. Similarly, the transport of neutral particles can be modeled either by computational fluid dynamics (CFD) or by kinetic methods such as the direct simulation Monte Carlo (DSMC) method.[53] The crucial criterion for the maximum tolerable cell size in the DSMC method is the mean free path, which implies a strong scaling of its numerical effort with total pressure. The advantage of the DSMC method is that it enables a direct description of particle transport and particle-wall interactions even under nonthermal conditions, while in CFD models, several assumptions, such as local diffusion coefficients, viscosity, turbulence models, etc., are required. For the investigations in this paper, a parallelized, combined DSMC/PIC-MC implementation, described in Ref. 54, is used. 3D PIC-MC simulations of a low pressure Ar discharge have already been reported in our cylindrical magnetron reactor.[55] The model has been shown to be a powerful tool to visualize and understand the influences of the magnetic field and the excitation mode on particles' motion and plasma parameters.

The article is organized into two parts. In the first part, CPA-based PPFs are deposited onto Si wafers at two different locations where the magnetic field strength strongly differs, namely, where plasma species densities and energies are different. The samples are analyzed by profilometry, x-ray photoelectron spectroscopy (XPS), time-of-flight secondary ion mass spectroscopy (TOF-SIMS) combined with principal component analysis (PCA), and ion beam analysis (IBA) to determine the influence of the magnetic field strength on the degrees of functionalization and cross-linking of the plasma layers. In the second part, after calculating electron impact cross sections of CPA through the R-matrix method,[56] two runs of 3D PIC-MC simulations are performed at

Published under license by AVS.

different levels of detail to track the behaviors of CPA ions and of the main radicals produced in the discharge. The simulations aim to bring new insights into how the different plasma species intervene in the plasma polymerization mechanisms and influence the resulting PPF properties.

II. EXPERIMENTAL SETUP

The plasma reactor has been extensively described in previous studies,[22,23,55] which are summarized in the recent review of Vandenabeele and Lucas.[57] In summary, the reactor consists of a cylindrical drum maintained on a grounded iron support, which contains a block of magnets. Gases are supplied through a gas shower located along the drum axis. Drum and gas shower are the electrodes of the system, made of stainless steel, electrically insulated from the rest of the setup, and connected to the poles of the power supply. The power supply operates in pulsed bipolar mode, as described in Ref. 55, except that off-times are 25 μs instead of 10 μs on each polarity. More precisely, each electrode is alternatively the cathode and the anode of the system. For each polarity, the power is applied during 10 μs (on-time), followed by 25 μs of off-time. The mean power dissipated in the discharge is 24 W (for both treatment and pretreatment), as calculated according to the method described in Ref. 55. The working pressure in the chamber is fixed at 10 Pa.

PPFs are deposited onto $1 \times 1\,\text{cm}^2$ pieces of Si wafers (Sil'tronix) that are placed at diametrically opposite positions in the middle of the drum, as shown in Fig. 1. Sample A is located at the bottom of the reactor, where the magnetic field strength has the highest value (~150 mTorr), while sample B is located at the top of the reactor, where the magnetic field is two orders of magnitude lower (~1.5 mTorr).[55] Initially, Si wafers are cleaned for 5 min in an Ar discharge with an Ar flow rate of 30 standard cubic centimeters per minute (SCCM) and a discharge power of 20 W using the same pulse scheme as described above. Subsequently, after evacuating Ar from the chamber, the deposition is carried out in pure CPA (98%, Sigma Aldrich, 15 SCCM) during 16 min.

The samples are first analyzed by profilometry and scanning electron microscopy (SEM) to measure the deposition rates and observe the PPF morphology at the two positions A and B. Then, XPS analyses are performed to measure the elemental composition and get a hint of the different chemical groups grafted into the PPFs. Next, TOF-SIMS analyses combined with PCA treatment are performed to observe the main chemical differences between both samples, particularly in terms of degrees of functionalization and cross-linking. Finally, IBA is used as a complementary tool, mainly to quantify the hydrogen content in the layers and confirm PCA results.

Deposition rates are measured by profilometry using a Dektak Veeco 8 stylus device and also estimated from SEM cross-sectional views by using a JEOL 6010LV microscope. XPS analyses are carried with a ThermoFisher K-Alpha photoelectron spectrometer (monochromatized Al K_α photon source, 1486.6 eV). Survey and high resolution spectra are recorded at pass energies of 200 and 30 eV, respectively, using a 250 μm diameter x-ray spot. High resolution spectra are fitted with Lorentzian–Gaussian components (L/G = 30%), with a full width at half maximum between 1.8 and 2.0 eV.

TOF-SIMS spectra are acquired by using a TOF-SIMS IV (Ion-Tof GmbH, Münster, Germany) spectrometer in the positive

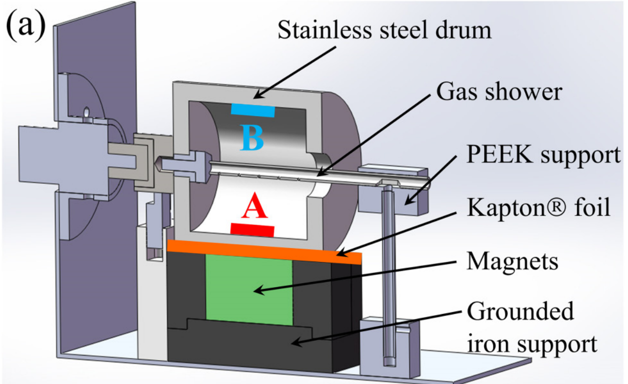

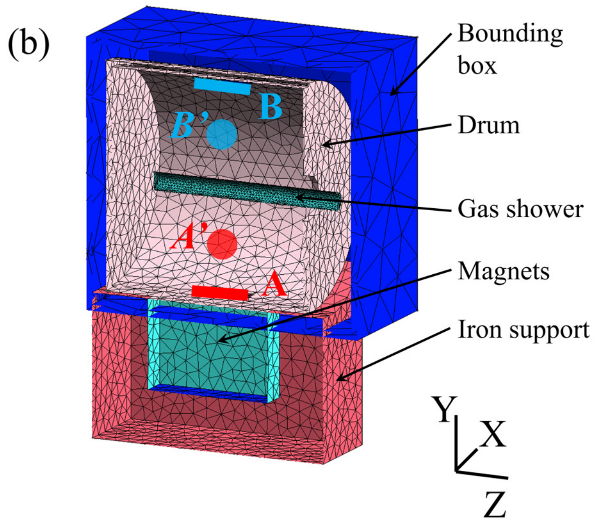

FIG. 1. (a) Scheme of the experimental set-up used for the deposition of PPFs, showing the two positions where PPFs have been analyzed. (b) Mesh geometry of the plasma reactor used for the PIC-MC simulations. *A′* and *B′* are 1 cm in diameter virtual spherical volumes where local densities have been numerically assessed.

mode by using a Bi_3^+ beam with a current of 0.35 μA at 25 keV, which is rastered over a $200 \times 200\,\mu\text{m}^2$ area. A low energy flood gun is used to ensure charge compensation and at least five points are analyzed for each sample. The calibration is done on CH^+, CH_3^+, and $C_2H_2^+$ peaks. After normalizing the peak intensities with respect to the total secondary ion count, the interpretation of TOF-SIMS spectra is done through the PCA method by using the NESAC/BIO Toolbox (Spectragui).[58]

To give some details about this method, PCA is a statistical method that allows to assess the main differences contained in a large amount of data. As well summarized by Cossement *et al.*,[5] PCA can be viewed as a projection method that turns an initial set of observations (e.g., TOF-SIMS spectra) of a n-dimensional system (n being the number of TOF-SIMS peaks considered) into a highly lowered dimensional system (two or three dimensions). The principal components (PC_i) are the axes of the new system and their

Published under license by AVS.

direction is calculated to display the maximum variance of the initial n-dimensional system. The PCA approach decomposes the initial system into a set of scores and loadings. The scores are the new coordinates of the observations (TOF-SIMS spectra) and correspond to the projection of the initial coordinates (intensities of the TOF-SIMS peaks considered) onto the different PC_i. The loadings give the statistical weight of contribution of the TOF-SIMS peaks to the PC_i. In this way, PCA analysis gives an overview, classification, and discrimination of the samples, as well as their chemical characterization. The reader can find a more detailed description of the PCA technique in Refs. 59 and 60.

IBA analyses are performed by combining elastic (non-Rutherford) backscattering spectroscopy (EBS) and elastic recoil detection analysis (ERDA). The analysis is done by using a 2.1 MeV ^{4}He beam with an intensity of about 3 nA. The sample under analysis is tilted at 65° relative to the incident beam direction such that the irradiated area is about $2.5 \times 1.0\,\text{mm}^2$. Data are recorded from three passivated implanted planar silicon detectors set at 165° and 135° (EBS-detectors) and 30° (ERDA-detector) with respect to the incident beam direction. The energy calibration of EBS-detectors is achieved from SnO_2/SiO_2 standard sample analysis, while the ratio between the ERDA and EBS detectors is derived from the analysis of a Kapton foil. The elemental depth profiles are obtained by fitting the ERDA and EBS spectra using DataFurnace[61] with the cross sections generated by SigmaCalc.[62]

III. SIMULATION MODEL SETUP

A. Cross-section calculations

We are unaware of previous electron collision cross sections for the CPA molecules. Therefore, to provide collision data for the PIC-MC simulations, collision cross sections between electrons and CPA molecules are computed via a combination of the binary encounter Bethe (BEB) and *ab initio* R-matrix methods by Quantemol Ltd. There are more electron-impact processes involving polyatomic molecules (like CPA) than those calculated here. In particular, electron impact vibrational excitation was not considered as such calculations on a system like CPA are not technically possible at present. Cross sections are calculated for the following electron-CPA collision processes:

Ionization:

$$C_3H_5NH_2 + e^- \rightarrow C_3H_5NH_2^+ + 2e^-. \tag{1}$$

Dissociative ionization:

$$C_3H_5NH_2 + e^- \rightarrow C_3H_5NH_2^- \rightarrow C_aH_bN_c^+ + C_nH_mN_p + 2e^-. \tag{2}$$

Electronic excitation:

$$C_3H_5NH_2 + e^- \rightarrow C_3H_5NH_2^* + e^-. \tag{3}$$

Rotational excitation:

$$C_3H_5NH_2(J = 0) + e^- \rightarrow C_3H_5NH_2(J) + e^-, \tag{4}$$

where $a + n = 3$, $b + m = 7$, and $c + p = 1$.

The total electron-CPA ionization cross section is calculated using *ab initio* BEB method,[63] which is a combination of Mott and Fowler[64] and Bethe[65] theories. Those theories describe, respectively, the hard, close collisions with small impact parameters, and the soft collisions with large input parameters. The BEB method accounts for both collision types and the BEB total ionization cross section is calculated according to

$$\sigma_{\text{BEB}} = \frac{S}{t + u + 1}\left(\frac{1}{2}\left(1 - \frac{1}{t^2}\right)\ln(t) + 1 - \frac{1}{t} - \frac{\ln(t)}{t + 1}\right), \tag{5}$$

where $t = T/B$, $u = U/B$, and $S = 4\pi a_0^2 N(R/B)^2$. T is the kinetic energy of the incident electron, B and U are the binding energy and average kinetic energy of the electrons in a subshell, respectively, N is the number of bound electrons, R is the Rydberg constant, and a_0 is the Bohr radius. Electron kinetic and binding energies of orbitals in the CPA molecule are calculated using the MOLPRO quantum chemistry software based on the Hartree–Fock (HF) approximation.[66] BEB cross sections have proved to be reliable for small organic molecules.[67,68]

Dissociative ionization cross sections are calculated by adapting Eq. (5) as follows:

$$\sigma_f = \frac{\Gamma_f S}{t_f + u + 1}\left(\frac{1}{2}\left(1 - \frac{1}{t_f^2}\right)\ln(t_f) + 1 - \frac{1}{t_f} - \frac{\ln(t_f)}{t_f + 1}\right), \tag{6}$$

where Γ_f is the branching ratio of the species and $t_f = \frac{T}{B - D_f}$, with D_f being the energy threshold at which the fragment f appears. To apply Eq. (6), one needs to know several parameters, namely the kinetic energy of the incident electron (T), the kinetic and binding energies of bound electrons (U and B), the energy thresholds at which each ionic fragment appears (D_f), and the branching ratios of each fragment (Γ_f). The energy threshold at which a dissociative ionization channel opens is equal to the ionization energy of the initial molecule plus the energy required to break all dissociating bonds minus the energy recovered by the formation of new bonds in the products. The energies considered for bond breaking or formation in the CPA dissociative channels are the binding energies found in the literature and are collected in Table I. The energy-dependent branching ratios of the different fragments are derived from the experimental cracking patterns of gaseous CPA measured by mass spectrometry for various values of electron energy (in the ionization source of the spectrometer), as described in Ref. 80. This method has so far been tested only for the NH_3 and NF_3 molecules, for which it was found to work well.[80]

Calculation of the electronic excitation cross sections is performed by using R-matrix radii of 13 a_o and Gaussian type orbitals to represent the continuum extending up to $l = 4$. Full description of the R-matrix method can be found in Refs. 56 and 81. Two different calculations that construct the inner region wavefunction are performed. The first is performed from orbitals computed by a complete active space consistent field (CASSCF) calculation made using a program MOLPRO (Ref. 66) and the second is performed using HF orbitals calculated using the R-matrix electron-scattering program UKRMOL.[82] The Quantemol-N expert system[83] is used to run the UKRMOL codes. The CASSCF wavefunctions freeze the [1–7 a′, 1–3 a″] orbitals,[78]

Published under license by AVS.

TABLE I. Energies for bond-breaking in nitrocarbons.

Type of bond	Instance of bond	Bond energy (eV)
C—H	C—H	3.513 (Refs. 69 and 70)
	HC—H	4.371 (Refs. 69–71)
	H_2C—H	4.900 (Refs. 69 and 70)
	NCH_2C—H	3.426 (Ref. 72)
	NC—H	5.594 (Ref. 73)
C—C	H_3C—CN	5.247 (Refs. 69 and 70)
	CH_3—CH_3	3.903 (Ref. 74)
C—N	C—N	7.589 (Refs. 69 and 70)
	H_3C—NH_2	3.426 (Refs. 69 and 70)
	H_5C_3—NH_2	3.118 (Ref. 75)
H—H	H—H	4.518 (Refs. 69 and 70)
N—H	N—H	3.686 (Refs. 69 and 70)
	HN—H	3.903 (Refs. 69 and 70)
	H_2N—H	4.510 (Refs. 69 and 70)
C=N	C=N	6.374 (Refs. 76 and 77)
C=C	C=C	6.288 (Refs. 78 and 79)
C≡C	NC≡CN	6.244 (Refs. 69 and 70)

TABLE II. Calculated vertical excitation energies (eV).

State	HF (6-311G*)	HF (cc-pVTZ)	CASSCF (6-311G*)	CASSCF (cc-pVTZ)
X $^1A'$				
a $^3A'$	8.045 997	8.075 928	6.571 215	6.758 964
A $^1A'$	8.405 169	8.380 680	7.251 465	7.387 515
b $^3A'$	9.455 475	9.441 870	8.489 52	9.403 776
c $^3A''$	9.485 410	9.460 917	8.777 946	9.558 873
B $^1A''$	9.684 039	9.635 061	11.771 05	9.635 061
C $^1A'$	9.697 644	9.659 550	11.784 65	9.367 782
d $^3A''$	9.738 459	9.694 923	12.908 42	10.203 750
D $^1A''$	9.945 255	9.874 509	12.951 96	10.451 361
e $^3A'$	10.032 33	9.947 976	12.973 73	10.560 201
E $^1A'$	10.266 33	10.152 051	13.205 01	10.576 527

put the remaining electrons in the active space [8–14 a′, 4–6 a″],[80] and explicitly include the $^1A'$ and $^3A'$ state configurations. Complete active space configuration interaction (CAS-CI) calculations[53] are then made with these orbitals, constructed from 6-311G* and cc-pVTZ basis sets. Table II shows the calculated vertical excitation energies. Excitation cross sections leaving CPA in the first four excited states a $^3A'$, A $^1A'$, b $^3A'$, and c $^3A''$ are taken from the calculation with orbitals constructed from a 6-311G* basis set and a CASSCF wavefunction. Inelastic cross sections to states with thresholds below the vertical ionization energy of 9.8 eV are taken from the calculation with a HF wavefunction with orbitals constructed from a 6-311G* basis set for consistency. The calculation of the electronic excitation cross sections must be regarded as the most uncertain part of the computations presented here and the ones presented represent what is possible to obtain with present methods. An extensive discussion of these issues is given by Brigg *et al.*[84]

Rotational inelastic cross sections from $J = 0$ to $J = 0–5$ are calculated using the POLYDCS code[85] with scattering, K-matrices up the first vertical excitation threshold of CPA, and orbitals constructed using cc-pVTZ orbitals. The molecular geometry of the CPA used for the calculation, shown in Table III, is taken from the NIST CCCBDB website.[86] Dipole moment of the target, equal to 1.19 D, is obtained from the available experimental data[87] and a Born correction is used for partial waves with l greater than 4 for the calculation of cross sections. Low energy rotational excitation is strongly controlled by the strength of the scattering dipole.[88] Thus, provided the experimental dipole is reliable, these cross sections should be accurate too.

The calculation of ionization and dissociative ionization cross sections is performed after calculating the threshold energies (Table II) for cation-radical fragments production and measuring their branching ratios by mass spectrometry. The calculation assumes that only one channel exists for the production of each set of cation-radical. Thresholds and branching ratios are summarized in Table IV.

The calculated dissociative ionization cross sections are shown in Figs. 2(a) and 2(b). The inelastic electron-CPA cross sections leaving CPA in specific excited states and the rotational excitation cross section up to $J = 0–5$ are shown in Figs. 2(c) and 2(d), respectively.

B. PIC-MC simulations

Particle-in-cell simulations combined with Monte Carlo collisions scheme (PIC-MC) are performed by using the PIC-MC/DSMC software package developed at Fraunhofer IST.[89–92] The open-source tool GMSH (Ref. 93) is used for the design of the reactor, as shown in Fig. 1(b), and also for the postprocessing. Before starting PIC-MC simulations, the magnetic field generated by the permanent magnets is computed by the boundary element method (BEM),[94] which is implemented in the same software as separate module. All magnetic parts—i.e., yoke and magnets—are represented by a

TABLE III. Geometry of CPA in the center-of-mass frame.

State	x (Å)	y (Å)	z (Å)
C	−0.32	−0.878	−0.7512
C	−0.32	−0.878	0.7512
C	−0.32	0.421	0.0
H	−1.2253	−1.1755	−1.2726
H	0.6085	−1.1458	−1.2463
H	−1.2253	−1.1755	1.2726
H	0.6085	−1.1458	1.2463
H	−1.2671	0.9693	0.0
N	0.908	1.1644	0.0
H	0.9523	1.768	−0.8168
H	0.9523	1.768	0.8168

Published under license by AVS.

TABLE IV. Threshold energies and branching ratios for cation-radical fragment production.

Cation-radical fragments	Branching ratio at energy (eV)				Threshold (eV)
	10	15	20	50	
$C_3H_5NH_2^+$	1	0.404	0.338	0.173	8.8
$C_3H_3 + NH_4^+$	0	0.016	0.043	0.054	9.75
$C_3H_4 + NH_3^+$	0	0.113	0.572	0.109	10.834
$NH_3 + C_3H_4^+$	0	0	0.129	0.017	10.834
$H_2 + C_3H_3NH_2^+$	0	0.024	0.036	0.023	11.134
$C_3H_5 + NH_2^+$	0	0	0.098	0.039	11.918
$NH_2 + C_3H_5^+$	0	0.003	0.204	0.027	11.918
$C_3H_4NH_2 + H^+$	0	0	0.055	0.008	12.226
$H + C_3H_4NH_2^+$	0.127	1	0.091	0.639	12.226
$C_3H_6 + NH^+$	0	0	0.053	0.049	12.395
$NH + C_3H_6^+$	0	0.007	0.117	0.023	12.395
$C_2H_3 + CH_3NH^+$	0	0.207	0.195	0.319	13.05
$NH_3 + H_2 + C_3H_2^+$	0	0	0.005	0.013	13.168
$2\ H_2 + C_3HNH_2^+$	0	0.008	0.015	0.013	13.468
$CH_2NH + C_2H_4^+$	0	0.157	0.5	0.5	13.653
$NH_2 + H_2 + C_3H_3^+$	0	0	0.063	0.053	14.252
$C_2H_4 + CH_2NH^+$	0	0.037	0.178	0.168	14.295
$H + H_2 + C_3H_2NH_2^+$	0	0.022	0.029	0.088	14.56
$CH_2NH_2 + C_2H_3^+$	0	0	0.367	0.055	14.741
$C_2H_5 + CNH_2^+$	0	0	0.5	0.5	14.827
$C_2H_2 + CH_3NH_2^+$	0	0.005	0.011	0.007	14.957
$C_2HNH_2 + CH_4^+$	0	0	0.098	0.039	15.448
$C_3H_3NH_2 + H_2^+$	0	0	0.266	0.055	15.652
$3\ H_2 + C_3HN^+$	0	0	0.015	0.014	16.539
$NH_2 + 2\ H_2 + C_3H^+$	0	0	0.002	0.007	16.586
$CH + C_2H_4NH_2^+$	0	0	0.021	0.004	16.727
$H + 2\ H_2 + C_3HNH^+$	0	0	0.015	0.025	17.371
$CH_2NH + H + H_2 + C_2H^+$	0	0	0.015	0.005	17.766
$C_3H_2NH_3 + CH_2^+$	0	0	0.005	0.013	17.95
$CH_2 + C_2H_3NH_2^+$	0	0	0.047	0.003	17.95
$C_2H_4 + H_2 + CNH^+$	0	0	0.367	0.055	18.632
$CH_2NH + H_2 + C_2H_2^+$	0	0	0.862	0.026	19.243
$C_2H_5 + H_2 + CN^+$	0	0	0	0.026	21.277

separate mesh; on its boundaries, a Laplace equation for the scalar magnetic potential is solved. From this solution, the magnetic field vector is obtained for each grid position in the region of interest (i.e., where the plasma simulation takes place). The magnetic material parameters are found in Table V. For the yoke, a high relative magnetic susceptibility of $\mu_Y = 5000$ yields an effective shortcut of the magnetic field. For $\mu_Y > 100$, the magnetic field solution is insensitive on its exact value. In the subsequent PIC-MC simulation runs, the BEM computed magnetic field is considered constant, namely, convection currents occurring in the plasma are assumed to cause negligible magnetic field contributions.

In order to keep the overall computational effort feasible, the PIC-MC simulations do not include a comprehensive plasma chemical model. Instead, only the electron impact cross sections with the CPA molecules and the six most important radical species resulting from dissociative ionization are taken into account. The first run assumes a total power of 10 W and uses a 3D simulation grid with 1 mm cell spacing. A physical time interval of three pulses (i.e., 210 μs) is computed, and only electrons, the CPA molecule and its ion are considered. The main purpose of the first simulation run is to identify the most frequent radical generation paths by dissociative ionization as well as the mean ion energy at different positions of the drum electrode. The second PIC-MC run is subsequently performed at a lower power of 1 W, which allows to use a larger spacing of the simulation grid of 1.5 mm and to increase the physical time interval to 1190 μs (17 pulses). Besides electrons and CPA molecules, the second run includes six more radicals, which either have the highest production rate, and/or which are especially of relevance with respect to surface functionalization. In the second run, secondary reactions between the reaction products (ions and radicals) are considered negligible and are not included in the model. However, momentum transfer cross sections between the generated species and CPA neutral molecules are included according to the variable soft sphere model.[53,95]

To investigate the power scaling influence on numerical results, two similar simulations at 1 and 10 W were compared during the first three electric periods (210 μs) to observe the power increase effect on plasma species densities and radical absorption on the reactor walls (results not shown). Increasing the power from 1 to 10 W leads to a higher average plasma density and to a reduced sheath thickness at the walls, but the spatial distributions of the generated species are nevertheless similar. Moreover, the averaged fluxes of radicals absorbed on the reactor walls are seen to scale linearly with power, namely, the absorption fluxes at 1 W are almost superimposable with the absorption fluxes at 10 W divided by 10. Consequently, we deduced that the general discharge behavior is not significantly modified by the power increase, and that 1 W simulations could be trustingly used to investigate the discharge properties at higher power.

The simulations are performed for studying the species generation on a qualitative basis. The present work does not aim to simulate the PPF growth. Consequently, most of surface processes, such as chemical reactions, progressive modification of surface conditions, surface diffusion, sputtering, implantation, heat transfer, etc., are neglected. However, to obtain information about the deposition rate distribution, a sticking coefficient was set for each species (Table V) and their absorption rates were monitored. Additionally, secondary electron emission is also included in the model.

IV. RESULTS

A. Experimental characterization of PPFs

The deposition rates are measured by profilometry and SEM. Both techniques give approximately the same values, namely, 27.2 ± 5.8 nm min^{-1} at position A and 10.6 ± 0.6 nm min^{-1} at position B. Thus, the deposition rates are about 2.57 times higher in the high magnetic field region. Figure 3 shows SEM cross sectional images of the two samples. At position B, the PPF is smooth and adheres well to the substrate. However, at position A, the PPF exhibits local delaminations.

The delamination of PPFs is described under different names in the literature, such as curling,[12] buckling,[96] or blistering.[97] This phenomenon is attributed to excessive stresses arising in the

Published under license by AVS.

FIG. 2. Calculated cross sections of (a) and (b) dissociative ionization, (c) electronic excitation, and (d) rotational excitation.

TABLE V. Physical and numerical parameters considered in the PIC-MC models.

Parameter	First run	Second run
Model dimension	$90 \times 90 \times 96\ \text{mm}^3$	$90 \times 90 \times 96\ \text{mm}^3$
Cell spacing	1 mm	1.5 mm
Magnetic remanence	1.22 T	1.22 T
Magnetic susceptibility	1.05	1.05
Yoke susceptibility	5000	5000
Species (sticking coefficient) (Ref. 17)	C_3H_7N, $C_3H_7N^+$, e^-	C_3H_7N (0), $C_3H_7N^+$ (1), e^- (1), CH_2NH (0.35), C_2H_5 (0.001), C_2H_3 (0.3), H (0.01), NH_2 (0.6), NH (0.11)
Time step width	1×10^{-12} s	1×10^{-11} s
Physical simulation time	210×10^{-6} s	1190×10^{-6} s
Number of CPU cores	20	20
Computation time	563 h	595 h

Published under license by AVS.

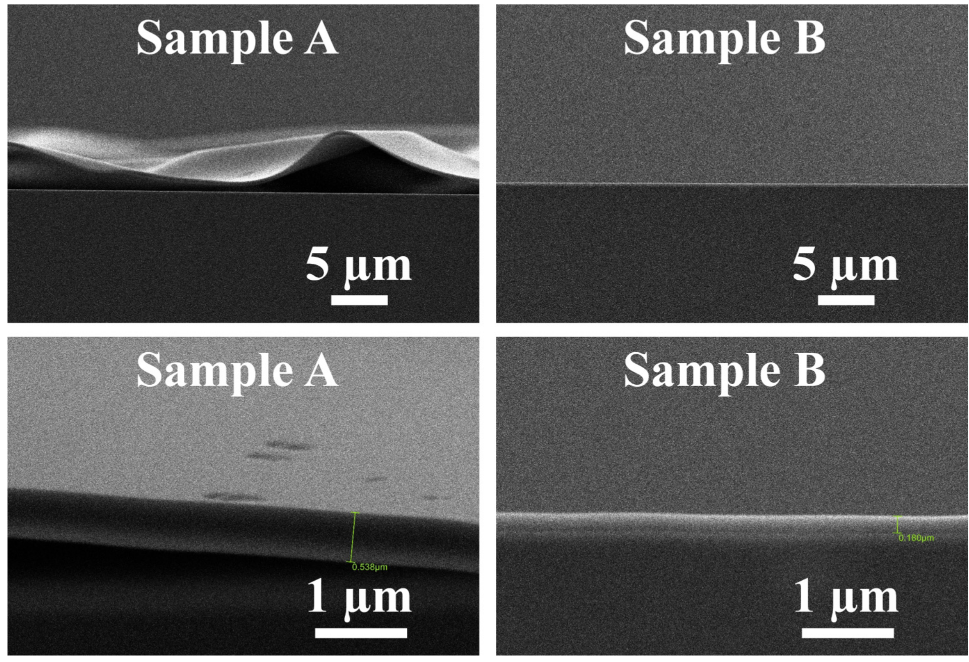

FIG. 3. SEM cross-sectional views of samples A and B.

coating under certain circumstances. First, the continuous adsorption of various building blocks combined with constant ion bombardment can generate a wedging effect leading to growth-induced internal stresses that increase with the layer thickness.[12,98] Second, the delamination can also be explained by a thermal expansion mismatch between the polymer layer and the substrate. Indeed, the thermal expansion coefficient of silicon ($2–4 \times 10^{-6}\,K^{-1}$) is much lower than the one of polymers (some tens to some hundreds of $10^{-6}\,K^{-1}$),[97] which can lead to post-treatment compressive stresses in the coating if the substrate undergoes significant heating during the deposition.[96] Third, postdeposition environmental attacks such as oxidation or moisture absorption can also induce stresses in the PPF, mainly in the case of porous coatings.[97,98] The delamination occurs when the stresses in the coating exceed the adhesive forces at the interface with the substrate. Based on these elements, the delamination at position A could be explained by a higher substrate heating induced by a stronger ion bombardment compared with position B. The heating of a surface subjected to ion bombardment is a largely known phenomenon in physical vapor deposition processes.[99,100] It results from the partial conversion of impinging ions kinetic energy into heat. This phenomenon is greatly exacerbated in low pressure conditions due to the greater ion mean free path and reduced surface cooling by heat transfer to the surrounding gas. This explains why the cathodes are generally water-cooled in magnetron discharges. As no cooling system is present in our low pressure discharge, the higher ion bombardment at position A could generate higher internal stresses and a higher substrate heating, resulting in a greater thermal expansion mismatch between the silicon substrate and the PPF.

The elemental composition of samples A and B measured by XPS is shown in Table VI, together with the corresponding [N]/[C] ratios. The oxygen detected is attributed to PPFs postplasma oxidation.[3] The [N]/[C] ratio ranges between 0.147 (sample A) and 0.161 (sample B). This ratio is lower than the one measured by XPS in other studies dealing with plasma polymerization of CPA, which can reach values between 0.2 and 0.26.[24,25,32] This difference is likely related to the difference in operating conditions and reactor design. Indeed, in the latter studies, the plasma is ignited by an RF power supply (13.56 MHz) and the substrate is kept at floating potential, while in our configuration, the excitation frequency is much lower (∼14.3 kHz) and the substrate is directly placed onto the high voltage electrode. Therefore, in our case, ions have more time to be accelerated by the applied electric field before the polarity reverses, and the substrate potential (between −400 and −500 V) is much higher (in absolute value) than the one reached in the case of floating surface (about −20 V for low pressure discharge). This leads to a much more intense surface ion bombardment during the deposition in our configuration. The link between lower nitrogen incorporation and stronger ion bombardment is also supported by the lower [N]/[C] ratio at position A (high magnetic field region) than at position B (low magnetic field region), as discussed later.

TABLE VI. Elemental concentrations of samples A and B measured by XPS.

Sample	Elemental concentrations (at. %)			[N]/[C]
	C1s	N1s	O1s	
Sample A	83 ± 0.6	12.2 ± 0.3	4.8 ± 0.7	0.147 ± 0.005
Sample B	82.5 ± 0.6	13.3 ± 0.2	4.2 ± 0.7	0.161 ± 0.005

Published under license by AVS.

To investigate with greater details the thin film chemistries at both positions, the XPS high resolution spectra of C1s and N1s peaks are fitted with three components corresponding to different bond configurations, as shown in Fig. 4. Assignments of the different components are done based on available literature[101] and the concentrations of the different contributions are gathered in Table VII.

Both samples exhibit quite close chemistries. Nevertheless, sample B shows a slightly higher content of primary/secondary amine (NH_x) groups and slightly lower content of nitrile (C≡N) and amide (N—C═O) groups compared to sample A. Also, sample A contains more C—C/C—H bonds and less CN bonds than sample B, which further confirms the lower nitrogen incorporation at position A.

To obtain further information about the thin film chemistry at positions A and B, the samples have been analyzed by TOF-SIMS. The resulting scores and loadings plots obtained after PCA analysis of the measured spectra are depicted in Fig. 5. The first two PCs displayed explain 99% of the overall variance, with 96% for PC_1 and 3% for PC_2. While no clear distinction can be done between both samples along the PC_2 axis, a marked difference is observed along the PC_1 axis. Indeed, the scores related to sample A are negative while the scores related to sample B are positive.

To determine the differences in terms of chemical composition between samples A and B, the scores plot has to be compared with the associated loadings plot depicted in Fig. 5(b). The loadings plot gives the contribution of the different TOF-SIMS peaks to the different PCs and enables us to identify the fragments responsible for the differences observed between the samples. From Fig. 5(b), we deduce that the fragments having m/z equal to 1 (H^+), 15 (CH_3^+), 27 ($C_2H_3^+$), 29 ($C_2H_5^+$), 39 ($C_3H_3^+$), 43 ($C_2H_5N^+$), 51 ($C_4H_3^+$), 52 ($C_3H_2N^+$), 63 ($C_5H_3^+$), 73 ($C_3H_7NO^+$), 75 ($C_6H_3^+$), and 87 ($C_7H_3^+$) are more representative of sample A because they have negative loadings. Similarly, the fragments at m/z equal to 18 (NH_4+), 30 (CH_4N^+),

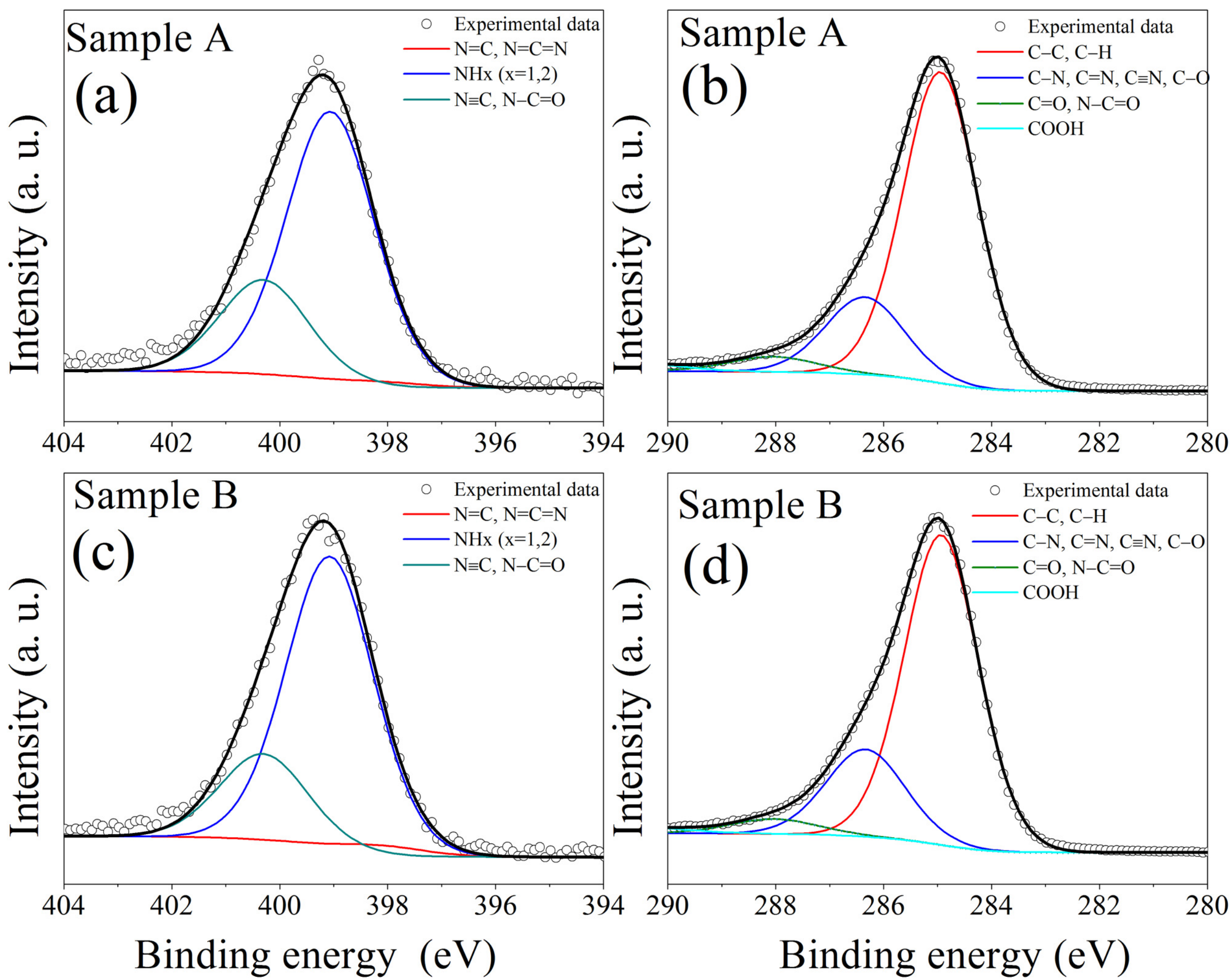

FIG. 4. XPS fitting of high resolution spectra of (a) N1s peak of sample A, (b) C1s peak of sample A, (c) N1s peak of sample B, and (d) C1s peak of sample B.

Published under license by AVS.

TABLE VII. Concentrations and characteristics of the different components used for fitting XPS high resolution spectra of C1s and N1s peak at positions A and B.

	Concentration (%)						
Element	C1s				N1s		
Position (eV)	285	286.5	288	289.5	398	399.2	400.5
Component	C—C C—H	C—N C=N C≡N C—O	C=O N—C=O	COOH	N=C N=C=N	NH_x	N≡C N—C=O
Sample A	74.1	19.6	4.3	2.0	1.2	73.1	25.7
Sample B	72.6	21.8	4.2	1.4	2.3	75.4	22.3

41 ($C_3H_5^+$), 42 ($C_2H_4N^+$), 43 ($C_3H_7^+$), 53 ($C_4H_5^+$), 55 ($C_4H_7^+$), 56 ($C_3H_6N^+$), 65 ($C_5H_5^+$), 68 ($C_4H_6N^+$), 70 ($C_4H_8N^+$), 77 ($C_6H_5^+$), 91 ($C_7H_7^+$), and 94 ($C_6H_8N^+$), which have positive loadings, better characterize sample B. From these data, it emerges that most of nitrogen-containing fragments have positive loadings and are therefore more present in sample B. Consequently, TOF-SIMS results corroborate XPS data, concerning the higher nitrogen incorporation in the PPF deposited at position B (low magnetic field region).

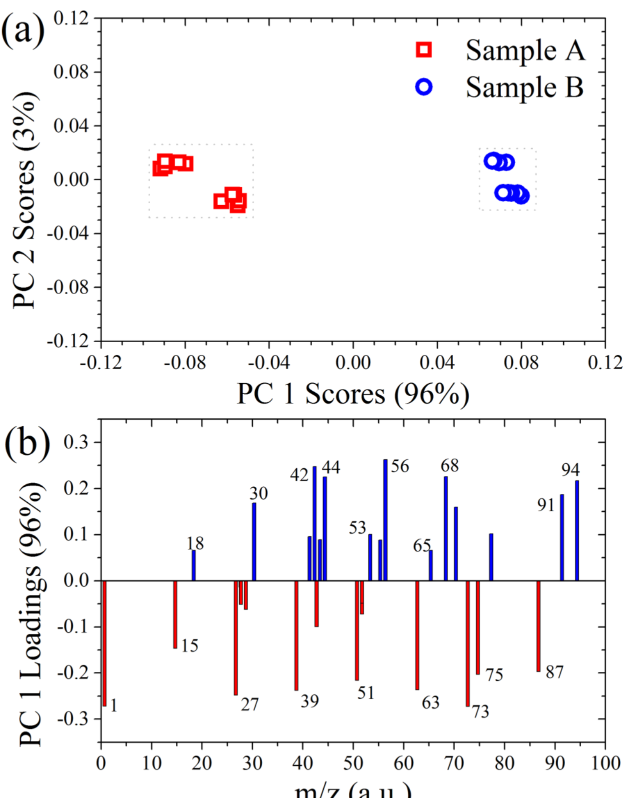

FIG. 5. (a) Scores plot and (b) loadings plot obtained from PCA analysis of TOF-SIMS spectra of samples A and B.

Information about the degree of cross-linking of the PPFs can also be extracted from PCA analysis by calculating an averaged $C_xH_y^+$ fragment from the most intense peaks of the loadings plot. Nitrogen-containing fragments are also considered for the calculation, by replacing each N atom by a CH group.[5] The resulting [C]/[H] ratio can be related to the unsaturated carbon content and to the degree of cross-linking. In the present case, the calculation gives a [C]/[H] ratio equal to 1.02 at position A and 0.67 at position B, which indicates a higher degree of cross-linking at position A (high magnetic field region). To summarize, TOF-SIMS analyses indicate that the nitrogen incorporation and the degree of cross-linking follow opposite trends depending on the magnetic field strength. The PPF deposition in the low magnetic field results in a higher nitrogen incorporation but a lower degree of cross-linking than in the high magnetic field region.

The higher degree of unsaturation at position A is also supported by IBA measurements. Elemental depth profiles determined with this technique are shown in Fig. 6. The corresponding elemental concentrations are gathered in Table VIII. The results show that elemental concentrations are constant throughout the PPFs depth. Moreover, the [C]/[H] ratio decreases by about 29% between positions A (2.05) and B (1.46), which is in good agreement with TOF-SIMS/PCA results, which give a drop in the [C]/[H] ratio of about 34% between positions A (1.02) and B (0.67). The differences observed between the two techniques in the calculation of the [C]/[H] ratio are likely due to the approximations made during PCA treatment. Indeed, in the last case, only the most influential TOF-SIMS peaks are considered (determined by statistical analysis), and N atoms are replaced by CH groups for the calculation. Despite these approximations, both techniques reveal close variations in [C]/[H] ratios between the two positions investigated and confirm the higher hydrogen deficiency at position A.

Moreover, as in the case of XPS analyses, the [N]/[C] ratio measured by IBA reveals a slightly higher nitrogen incorporation at position B than at position A, with good agreement between the two techniques (+9% for XPS, +7% for IBA). Nevertheless, [N]/[C] ratios measured by IBA are substantially higher than the ones measured by XPS (e.g., 0.27 instead of 0.147 at position A). This difference is likely related to the different depths of analysis between the

Published under license by AVS.

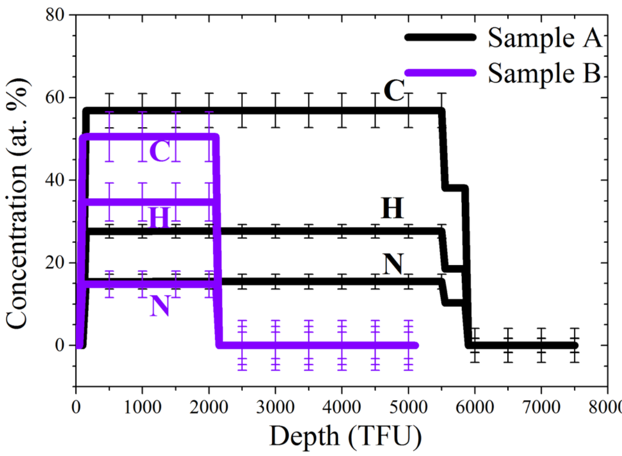

FIG. 6. Elemental depth profiles of samples A and B measured by IBA.

two techniques. Indeed, XPS only analyzes the first 5–10 nm of the surface and is more sensitive to carbon contamination, while IBA scans the whole samples depth.

As the IBA technique indicates the number of atoms per square centimeter for each element present in the PPF, it is possible to deduce the mass of each element per square centimeter, and ultimately, by dividing the result by the PPF thickness, to obtain the "partial density" (in g cm^{-3}) for each thin film constituent. The sum of all "partial densities" allows determining PPF density at the different positions investigated. By doing so, we measure PPF densities of 2.0 ± 0.4 g cm^{-3} at position A and 1.7 ± 0.3 g cm^{-3} at position B. These values are markedly higher than the ones measured in the literature for PPFs synthesized from CPA or its allylamine isomer in similar power conditions, which range between 1.1 and 1.5 g cm^{-3}.[26,102] Once again, this difference could be explained by our different reactor geometry and excitation mode, which would lead to a more intense ion bombardment during the PPF growth. Such a bombardment would lead, in turn, to stronger PPF sputtering and hydrogen abstraction, generating more dangling bonds on the polymer surface, resulting in a higher degree of cross-linking and PPF density after thin film restructuring.

B. Plasma simulations

The first run of plasma simulation is performed with C_3H_7N, $C_3H_7N^+$, and e^- as reactive species, by implementing the calculated cross sections. Besides tracking the production rates of

TABLE VIII. Elemental concentrations of samples A and B measured by IBA.

Sample	Elemental concentrations (at. %) C	N	H	[C]/[H]	[N]/[C]
Sample A	56.9 ± 4.1	15.4 ± 1.8	27.7 ± 1.6	2.05	0.27
Sample B	50.5 ± 6	14.8 ± 3.3	34.7 ± 4.6	1.46	0.29

radicals, $C_3H_7N^+$ ion properties are investigated. Figure 7 depicts the spatial distribution of the electric potential, electron and ion densities, and ion energy averaged over a negatively polarized drum period of 10 μs (between 141 and 150 μs, when ions are directed to the drum), in order to study the ions' behavior at positions A and B during PPF deposition.

From Figs. 7(d) and 7(e), the average ion energy near magnets (position A) is about 35% higher than in the opposite position (position B). The reason is likely related to the magnetic field lines, which are responsible for a slight depletion in charged species densities near position A [Figs. 7(b) and 7(c)]. Thus, ions reaching this position are more likely originating from central positions of the reactor. Therefore, ions reaching the wall at position A have – in average – seen a greater potential difference compared to ions hitting other wall regions.

According to volume and time averaged collision statistics determined during the first simulation run, the radicals mostly generated in the plasma (and corresponding threshold energies) are H (12.226 eV), CH_2NH (13.653 eV), C_2H_5 (14.827 eV), and C_2H_3 (13.050 eV). These radicals have thus been considered in the second simulation run to study their spatial generation and diffusion inside the plasma reactor. Additionally, NH_2 and NH radicals have been included in the second run, because they are expected to contribute to surface functionalization. For each of the radicals, a sticking coefficient taken from the work of Mao and Bogaerts[17] is attributed (Table V), in order to track their absorption on the reactor walls, notably at positions A and B. The sticking coefficient of $C_3H_7N^+$ ions is assumed to be unity,[17,103] while a sticking coefficient of 0 is used for CPA molecules, because they are considered to be reflected at the walls.[17]

The spatial density distributions of the different radicals investigated, of electrons and $C_3H_7N^+$ ions, are depicted in Fig. 8. These distributions are averaged over the two last periods of the plasma simulation, namely, from the 15th to the 17th period (1050–1190 μs). For all radicals [Figs. 8(a)–8(f)], the generation mainly takes place around the gas shower and near magnets edges, as a result of the higher electron densities (and thus collision rates) in these areas [Fig. 8(g)]. Similarly, areas of highest ion density coincide with those of highest electron densities.

To compare in a more quantitative way the densities of the different species, two 1 cm in diameter virtual spherical volumes, named A' and B', located in the middle of the drum along the z axis and halfway between the gas shower and positions A and B, respectively, have been defined [Fig. 1(b)]. The average densities of the different species calculated in these two volumes during the period 1050–1190 μs are gathered in Table IX. Average densities are systematically higher in volume A' than in volume B', as a result of the electron magnetic confinement near magnets, which leads to higher collision rates. Nevertheless, as neutral radical species are not directly affected by electromagnetic fields and can diffuse more freely in the reactor, the average densities of radicals are only 1.2–1.4 times higher in volume A' than in B', while they are 2.3–2.5 times higher in the case of charged species.

The radicals are produced in different proportions inside the reactor, the most produced being CH_2NH and C_2H_5, while NH and NH_2 are generated in significantly lower quantities. For example, the average density of CH_2NH radicals is more than 22 times higher than the one of NH radicals, for both volumes

Published under license by AVS.

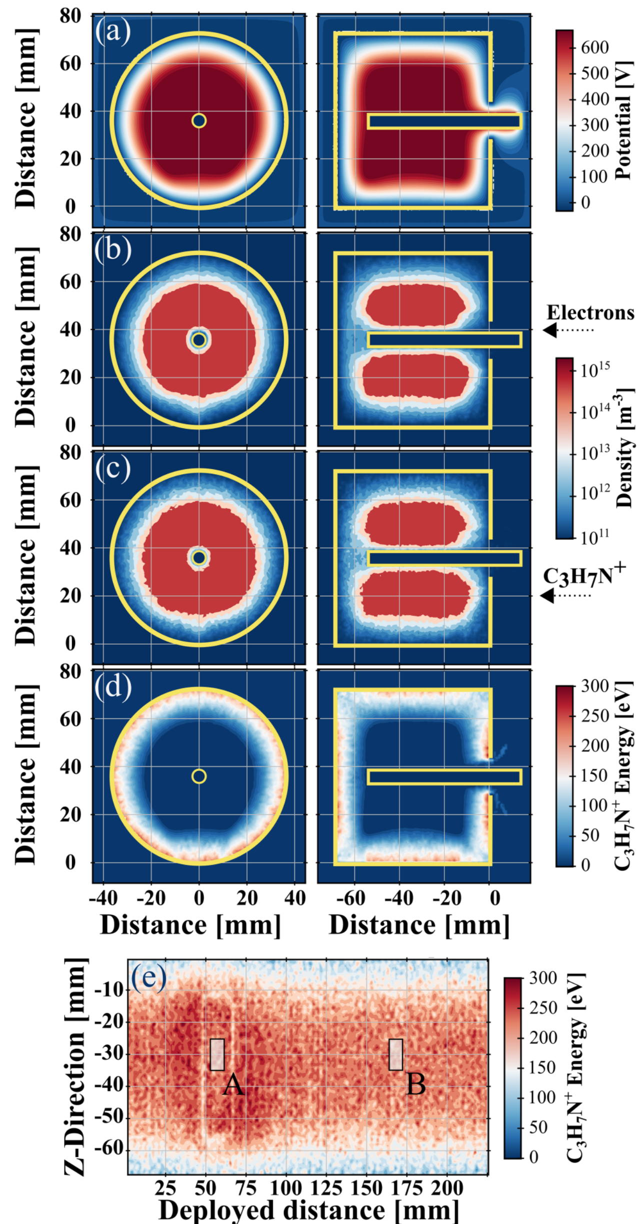

FIG. 7. Face view and side view of the spatial distribution of (a) electric potential, (b) electron density, (c) $C_3H_7N^+$ density, and (d) $C_3H_7N^+$ energy averaged over 10 μs (between 141 and 150 μs). (e) Corresponding 2D energy mapping of $C_3H_7N^+$ ion reaching the unrolled drum surface. The 0 position on the *x* axis relates to the leftmost position of the drum in the xy plane. The two positions A and B, where 1 × 1 cm^2 Si wafers have been placed for experimental investigations, are indicated by small rectangles.

considered. Another notable feature is that the densities of the main radicals are about 100 times higher than the ones of charged species, which rapidly decrease during off times, while radical densities are barely affected by discharge pulses.

To visualize the influence of discharge pulses on the behavior of the different species and investigate in deeper details how these species contribute to the thin film growth, 2D absorption mappings are shown in Fig. 9. Displayed data are averaged over the different ON and OFF times of the two last periods (1050–1190 μs). More precisely, $T_{1\text{-ON}}$ stands for absorption values averaged over the first ON time (negative drum) of the two last periods, namely, during 1050–1060 and 1120–1130 μs. Similarly, $T_{1\text{-OFF}}$ stands for absorption values averaged over the first OFF times (1060–1085 and 1130–1155 μs), $T_{2\text{-ON}}$ stands for absorption values averaged over 1085–1095 and 1155–1165 μs (second ON time with negative drum), and $T_{2\text{-OFF}}$ over 1095–1120 and 1165–1190 μs. The different mappings correspond to the unrolled drum surface, with the 0 position on the *x* axis relating to the leftmost position of the drum in the xy plane. Following this notation, sample A is located around x = 56 mm and sample B around x = 168 mm, as indicated by the rectangles added in Fig. 9. More quantitative data are given in Fig. 10, which shows more precisely the average absorption values at positions A and B.

From Figs. 9 and 10, we see that radicals and ions mainly absorb around magnets edges (around A), and to a lower extent, at the opposite position (around B). The most absorbed radicals on the drum surface are H, C_2H_3 and CH_2NH, while NH and NH_2 absorb to a much lower extent. Despite its high production rate, C_2H_5 is the least absorbed radical due to its very low sticking coefficient (0.001). Conversely, despite its low sticking coefficient (0.01), H is highly absorbed at both positions due to its high density and probably higher mobility.

Additionally, while radicals are almost insensitive to discharges pulses, charged species strongly depend on the drum polarity. Indeed, radicals absorb on the drum surface in similar extents during ON and OFF times, whatever the polarity, because OFF times are too short for radicals to relax significantly between two ON times. Moreover, radicals' motion is not influenced by the applied electric field. On the contrary, $C_3H_7N^+$ ion absorption mainly occurs during ON times with negative drum. During these periods, the average absorption values of $C_3H_7N^+$ ions are about 10 times higher than the one of the main radicals.

To better compare the relative contributions of ions and radicals to the PPF growth, time-weighted average absorption values are also indicated in Fig. 10. For both positions, these values are strongly reduced compared with those during negatively polarized drum periods, but they are still higher than the ones of radicals, indicating that ions strongly contribute to the mass deposited.

An interesting observation is that average absorption rates of C_2H_3 radicals, CH_2NH radicals, and $C_3H_7N^+$ ions (namely, three of the most absorbed species) are, respectively, 2.33, 2.26, and 2.21 times higher at position A than at position B. These values are very close to the ratio between the experimental deposition rates measured at positions A and B, namely, 2.57. Conversely, the absorption rate of H radical (one of the two most absorbed radicals) is only 1.33 times higher at position A than at position B, but this species is not expected to contribute significantly to the mass deposited. Nevertheless, a second interesting point is that this ratio is close to the one between the [H]/[C] ratio at position B (34.7/50.5 = 0.687) and the [H]/[C] ratio at position A (27.7/56.9 = 0.487) determined by IBA (cf. Table VIII), namely, 0.687/0.487 = 1.41, although the trend goes in the opposite direction.

Published under license by AVS.

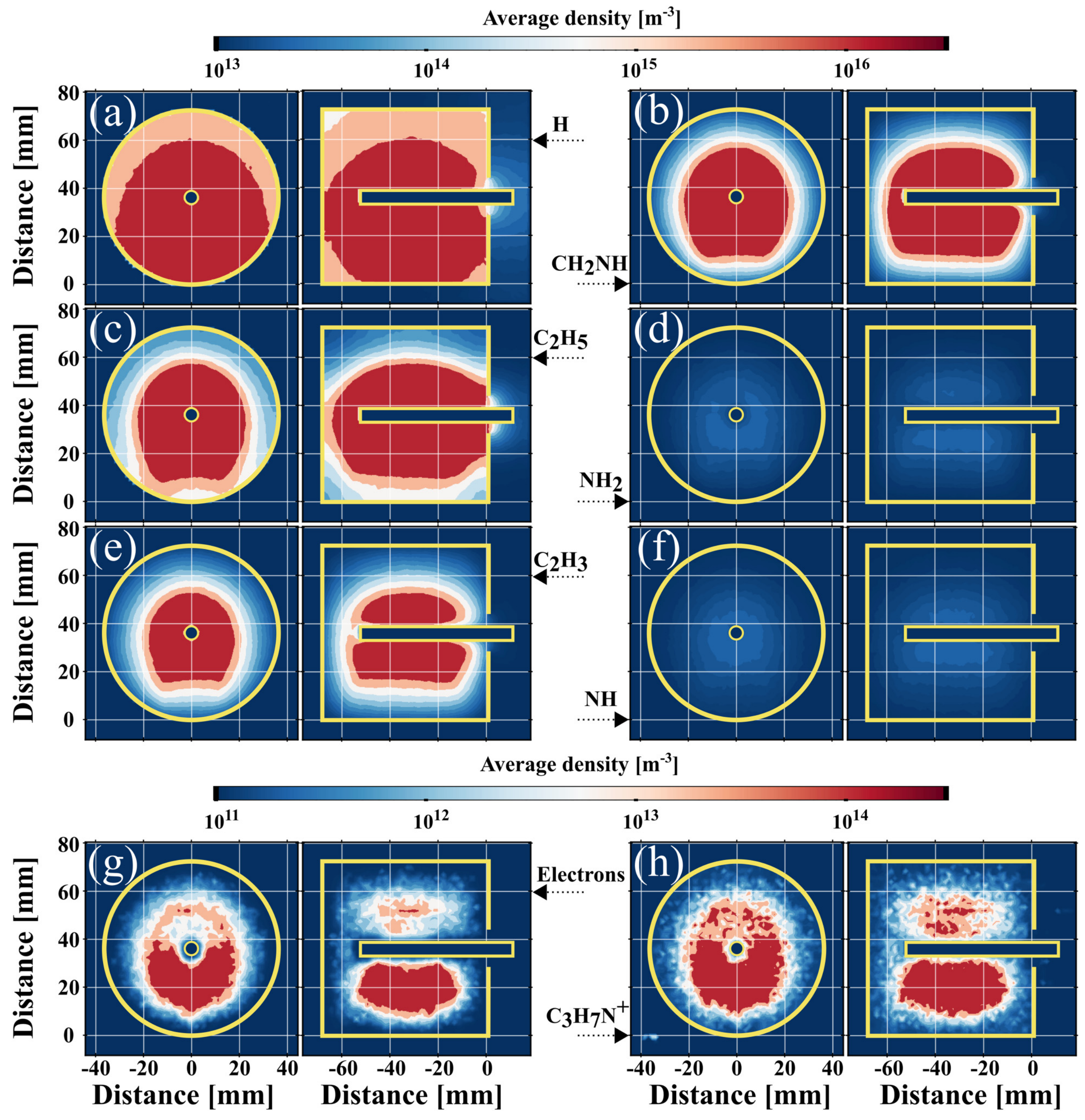

FIG. 8. Face view (left) and side view (right) of the spatial density distribution of (a) H, (b) CH_2NH, (c) C_2H_5, (d) NH_2, (e) C_2H_3, and (f) NH radicals, of (g) electrons and (h) $C_3H_7N^+$ ions. The displayed data are averaged over two periods, from the 15th to the 17th period (1050–1190 μs). Let us note that color gradient bars are different for radicals and charged species due to the much smaller densities of the latters.

V. DISCUSSION

The plasmas generated in the cylindrical magnetron reactor described in this study are highly nonuniform due to the presence of strong magnetic field gradients. As seen in our previous study[55] and in the present work, these gradients are responsible for spatial variations in plasma parameters, such as electron density and temperature, ion density and energy, radical density and distribution, and absorption rates.

Published under license by AVS.

TABLE IX. Average densities of the different species calculated over two periods, from 1050 to 1190 μs, in two volumes A′ and B′ defined in Fig. 1(b).

Species	Average densities ($\times 10^{14}$ m^{-3})							
	H	C_2H_5	C_2H_3	CH_2NH	NH	NH_2	e^-	$C_3H_7N^+$
A' volume	309	420	255	378	18.6	20.2	4.35	4.50
B' volume	265	330	192	289	13.8	14.8	1.73	1.95

Therefore, the PPFs produced from depositing organic vapors exhibit strong changes in their properties depending on the position considered on the drum surface. In this work, we considered two different positions A and B, near magnets and at the opposite position, indicated in Fig. 1, where the magnetic field has, respectively, its highest and lowest values. We used complementary analytical techniques among profilometry, SEM, XPS, TOF-SIMS/PCA, and IBA to study the properties of thin films deposited from CPA in a pulsed bipolar discharge. We showed that besides the deposition rates 2.57 times higher near magnets, the PPF deposited at position A exhibit a different morphology and chemistry.

More precisely, PPFs deposited in the high magnetic field region show important delaminations (Fig. 3), a lower nitrogen incorporation (Table VI), a higher percentage of multiple CN bonds, such as nitrile groups, at the expense of amine functionalities (Fig. 4 and Table VII), a lower hydrogen content (Fig. 6), a higher degree of cross-linking, and a thin film density about 20% higher. We suspected that the main reason for such a different behavior was the more energetic conditions at position A, with notably a higher precursor fragmentation and a higher ion bombardment enhanced by the stronger magnetic field. Indeed, a higher fragmentation could lead to a greater number of thin film-forming species, explaining the higher deposition rates, but also to smaller depositing fragments, resulting in a denser and less flexible coating, less suited to counteract stresses at the interface. Internal stresses in the coating could be magnified by a more intense ion bombardment, providing more energy to dissipate, as well as a greater thermal expansion mismatch caused by a stronger substrate heating. Additionally, the higher ion bombardment could break more chemical bonds on the growing film surface, releasing hydrogen and nitrogen atoms in the gas phase, and generating more dangling bonds, accelerating the deposition rates, and increasing the degree of cross-linking and the number of multiple bonds, as also observed in previous studies.[32,33,104]

To confirm these hypotheses and better understand the plasma polymerization mechanisms in this particular reactor configuration, we performed 3D PIC-MC simulations of a CPA discharge in the cylindrical magnetron reactor. Due to the huge number of reactions occurring in a plasma polymerization process from a molecule as complex as CPA, several considerations and approximations were made to enable the use of the 3D PIC-MC tool to extract information about thin film growth mechanisms. Indeed, take into account all possible physicochemical processes (numerous collisions leading to various fragmentation pathways, to the ionization and rotational, vibrational, electronic transitions of the CPA molecule and its fragments, emission of energetic photons able to intervene in subsequent processes, chemical reactions occurring between all generated species, both in gas phase and on reactor walls, surface processes such as adsorption, diffusion, secondary electron emission, reactive etching, and sputtering or ion implantation) would require unrealistic numerical resources and computing times.

Therefore, we decided to perform two simulation runs. The first one aimed at studying the behavior of the CPA ion (supposed to be the majority ion due to the abundance of CPA molecules compared to other species and to the relatively low ionization energy of the CPA molecule) and determining the main radicals produced in the discharge in power conditions as close as possible from the one used experimentally. The goal of the second run was to study the diffusion and absorption on reactor walls of the main species. As substrate heating and deposited material was assumed negligible on computing timescale involved (1.2 ms), constant sticking coefficients (taken from the literature) were considered. This modus operando enabled us to confirm experimental assumptions and to provide inputs for discussion regarding plasma polymerization processes.

Indeed, numerical results showed that ion density is 2.3–2.5 times higher in the vicinity of position A compared to position B (Table IX), due to the higher electron density that leads to higher ionization rates. Moreover, ions reaching position A are 35% more energetic than ions reaching B (Fig. 7). This clearly supports the stronger ion bombardment near magnets previously discussed. The distribution of radicals in the reactor is more homogeneous than the one of charged species (Table IX), because they are insensitive to the discharge pulses and polarity. However, their production is spatially dependent on electron distribution (Fig. 8).

We showed that the main radicals produced in the CPA discharge are H, CH_2NH, C_2H_3, and C_2H_5. NH and NH_2 radicals, which were expected to contribute significantly to surface functionalization, are produced to a much lower extent (Fig. 8), leading to very low absorption rates (Figs. 9 and 10). Nevertheless, the abundance of certain radicals does not necessarily mean that they play an important role in the PPF growth. For example, C_2H_5 is the main species formed in the discharge, but its absorption rate is paltry due to its very low sticking coefficient.

An important result is that the ratios between the absorption rates of the most absorbing species (CH_2NH, C_2H_3, and $C_3H_7N^+$) at position A and the ones at position B (between 2.21 and 2.33) are very close to the ratio between the deposition rates experimentally measured at the same positions (2.57) (Fig. 10). This indicates that absorption rates are important data to determine the species actively taking part to the thin film growth. For H radicals, the ratio between absorption rates at position A and at position B is only 1.33 (Fig. 10), but hydrogen is not suspected to contribute significantly to the mass deposited. Interestingly, this ratio is very close to the inverse of the ratio between the [H]/[C] ratio measured by IBA

Published under license by AVS.

FIG. 9. 2D absorption mappings on the unrolled drum surface averaged over the different ON and OFF times of the two last periods of the plasma simulation (1050–1190 μs) for (a) H radicals, (b) NH_2 radicals, (c) NH radicals, (d) C_2H_3 radicals, (e) C_2H_5 radicals, (f) CH_2NH radicals, (g) $C_3H_7N^+$ ions, and (h) electrons. The 0 position on the *x* axis relates to the leftmost position of the drum in the xy plane. The two positions A and B, where 1 × 1 cm^2 Si wafers have been placed for experimental investigations, are indicated by small rectangles.

Published under license by AVS.

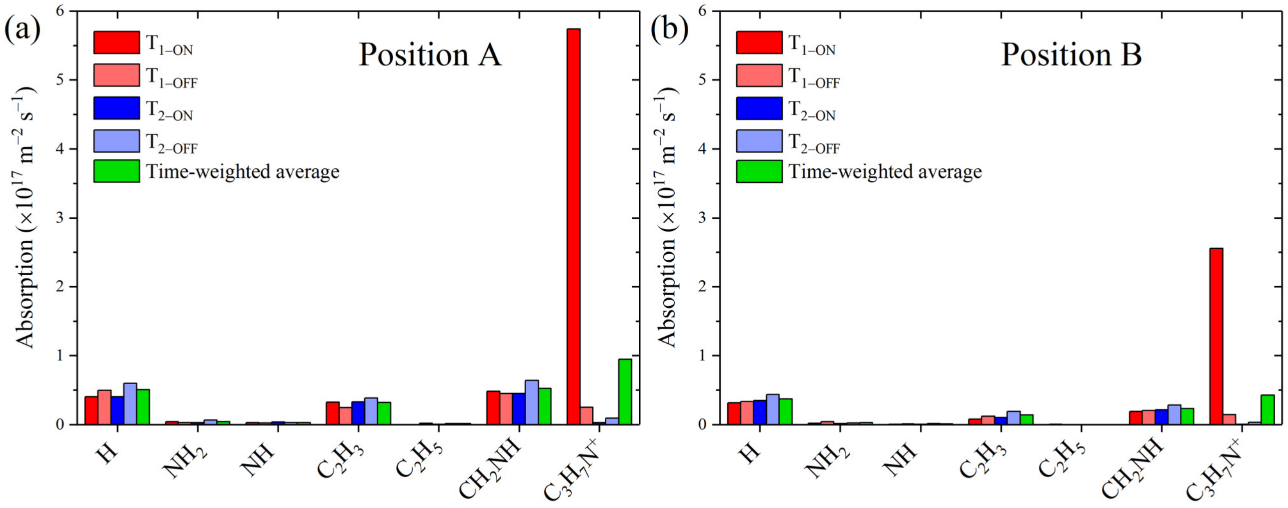

FIG. 10. Average absorption values over the different ON and OFF times of the two last periods of the plasma simulation (1050–1190 μs), at (a) position A and (b) position B.

at position A and the [H]/[C] ratio measured at position B, namely, 0.487/0.687 = 1/1.41 (Table VIII). This could indicate that, instead of contributing to the thin film growth, atomic hydrogen adsorbed on the growing film could be responsible for hydrogen abstraction from the PPF, by generating molecular dihydrogen released in the gas phase, following an Eley–Rideal mechanism.[105,106]

The lower [N]/[C] ratio at position A compared with position B could possibly be explained by a similar process, or also following a Langmuir–Hinshelwood mechanism (migration of two adsorbed atoms on the surface followed by the formation of a molecule that desorbs in the gas phase),[105] which could be enhanced at position A by the stronger ion bombardment that brings more energy and magnifies surface diffusion. Another explanation could be a greater fragmentation of the CPA molecule in the volume adjacent to position A due to the higher electron density near magnets, leading to a lower retention of CN bonds. Indeed, it was previously shown that the presence of CN bonds in the precursor (or depositing fragments) was important for a greater nitrogen incorporation.[32,33] Nevertheless, the results presented in this work do not enable us to support this hypothesis, because the two species retaining the CN bond among tracked species (CH_2NH and $C_3H_7N^+$) stay more abundant near position A than near position B.

The most interesting point of the present work is that it allows to discuss the respective roles of ions and radicals in PPF growth mechanisms, roles that are actively debated in the literature.[4,7,16] Indeed, our results confirm that even if the ion density in the gas phase is about 100 times lower than the density of the main radicals (Table IX), adsorption of ionic species on the growing PPF can be up to 10 times higher than radicals adsorption when they are accelerated toward the surface (Fig. 10). Nevertheless, ions are very sensitive to discharge pulses and polarity and their role is significantly reduced during OFF times because they are rapidly neutralized (Fig. 9). Conversely, radicals consistently take part to the thin film growth throughout the process duration. Consequently, the respective roles of ions and radicals toward a plasma polymerization process strongly depend on the reactor geometry and on the applied signal parameters.

VI. CONCLUSIONS

In this study, we performed a combined experimental and numerical study of a cyclopropylamine plasma in a low-pressure cylindrical magnetron reactor. We showed that the magnetic field strength strongly influences the final PPF properties, such as deposition rates, adherence, roughness, density, and degrees of functionalization and cross-linking.

To investigate plasma polymerization mechanisms, we performed for the first time 3D PIC-MC simulations of the CPA discharge after computing electron-cyclopropylamine collision cross sections using the R-matrix method. Due to the complexity of the plasma polymerization process and the computational times and resources required for 3D PIC-MC numerical study, several assumptions and simplifications have been done to perform the simulations on a feasible timescale. Nevertheless, the presented results enabled us to determine the main radicals formed in the discharge and visualize their spatial distribution, to assess the energy of ions impacting the substrate, to correlate the numerically calculated absorption rates with experimentally measured deposition rates, and to investigate the contribution of ions and radicals toward thin film growth. We showed that despite their strongly different production rates, both ions and radicals significantly contribute to the mass deposited, but their respective roles are strongly dependent on the reactor geometry and discharge parameters.

Therefore, we showed that 3D PIC-MC simulations are a powerful tool to bring new insights into plasma polymerization

Published under license by AVS.

mechanisms and to possibly quantify phenomena in reactor configurations where measurements are difficult to perform.

ACKNOWLEDGMENTS

The authors gratefully acknowledge the financial support of the Walloon Region under the Flycoat Project (No. 1318147). For all simulations, computational resources were provided by the Consortium des Équipements de Calcul Intensif (CÉCI), funded by the Fonds de la Recherche Scientifique de Belgique (F.R.S.-FNRS) under Grant No. 2.5020.11. The authors would like to thank Dan Graham for developing the NESAC/BIO Toolbox used in this study and the NIH grant (No. EB-002027) for supporting the toolbox development. The authors also thank Céline Noël and Alexandre Felten for their assistance in the TOF-SIMS experiments and Paul-Louis Debarsy and Julien Colaux for their assistance in performing IBA experiments. The authors also acknowledge the SIAM platform of the University of Namur.

REFERENCES

[1]A. Choukourov, H. Biederman, D. Slavinska, L. Hanley, A. Grinevich, H. Boldyryeva, and A. Mackova, J. Phys. Chem. B **109**, 23086 (2005).
[2]H. J. Griesser, R. C. Chatelier, T. R. Gengenbach, G. Johnson, and J. G. Steele, J. Biomater. Sci. Polym. Ed. **5**, 531 (1994).
[3]K. S. Siow, L. Britcher, S. Kumar, and H. J. Griesser, Plasma Process. Polym. **3**, 392 (2006).
[4]F. Khelifa, S. Ershov, Y. Habibi, R. Snyders, and P. Dubois, Chem. Rev. **116**, 3975 (2016).
[5]D. Cossement, F. Renaux, D. Thiry, S. Ligot, R. Francq, and R. Snyders, Appl. Surf. Sci. **355**, 842 (2015).
[6]J. Dorst, M. Vandenbossche, M. Amberg, L. Bernard, P. Rupper, K. D. Weltmann, K. Fricke, and D. Hegemann, Langmuir **33**, 10736 (2017).
[7]D. Thiry, S. Konstantinidis, J. Cornil, and R. Snyders, Thin Solid Films **606**, 19 (2016).
[8]S.-H. Seo, J.-H. In, and H.-Y. Chang, Plasma Sources Sci. Technol. **13**, 409 (2004).
[9]S.-H. Seo, J.-H. In, H.-Y. Chang, and J.-G. Han, J. Appl. Phys. **98**, 043301 (2005).
[10]P. Sigurjonsson and J. T. Gudmundsson, J. Phys. Conf. Ser. **100**, 062018 (2008).
[11]M. Shen and A. T. Bell, "A review of recent advances in plasma polymerization," in *Plasma Polymerization* (American Chemical Society, Washington, DC, 1979), Vol. 108, p. 1.
[12]H. Yasuda, *Plasma Polymerization* (Academic, Orlando, FL, 1985).
[13]R. d'Agostino, *Plasma Deposition, Treatment, and Etching of Polymers* (Academic, San Diego, CA, 1990).
[14]A. Michelmore, P. Gross-Kosche, S. A. Al-Bataineh, J. D. Whittle, and R. D. Short, Langmuir **29**, 2595 (2013).
[15]A. J. Beck, S. Candan, R. D. Short, A. Goodyear, and N. S. J. Braithwaite, J. Phys. Chem. B **105**, 5730 (2001).
[16]A. Michelmore, J. D. Whittle, and R. D. Short, Front. Phys. **3**, 3 (2015).
[17]M. Mao and A. Bogaerts, J. Phys. D Appl. Phys. **43**, 205201 (2010).
[18]S. Candan, A. J. Beck, L. O'Toole, R. D. Short, A. Goodyear, and N. St. J. Braithwaite, Phys. Chem. Chem. Phys. **1**, 3117 (1999).
[19]D. B. Haddow, R. M. France, R. D. Short, J. W. Bradley, and D. Barton, Langmuir **16**, 5654 (2000).
[20]A. Michelmore, D. A. Steele, D. E. Robinson, J. D. Whittle, and R. D. Short, Soft Matter **9**, 6167 (2013).
[21]D. Hegemann, E. Körner, N. Blanchard, M. Drabik, and S. Guimond, Appl. Phys. Lett. **101**, 211603 (2012).
[22]C. Rigaux, F. Tichelaar, P. Louette, J. L. Colaux, and S. Lucas, Surf. Coat. Technol. **205**, S601 (2011).
[23]S. Mathioudaki, B. Barthélémy, S. Detriche, C. Vandenabeele, J. Delhalle, Z. Mekhalif, and S. Lucas, ACS Appl. Nano Mater. **1**, 3464 (2018).
[24]L. Denis, P. Marsal, Y. Olivier, T. Godfroid, R. Lazzaroni, M. Hecq, J. Cornil, and R. Snyders, Plasma Process. Polym. **7**, 172 (2010).
[25]A. Manakhov, L. Zajíčková, M. Eliáš, J. Čechal, J. Polčák, J. Hnilica, Š Bittnerová, and D. Nečas, Plasma Process. Polym. **11**, 532 (2014).
[26]A. Manakhov, P. Skládal, D. Nečas, J. Čechal, J. Polčák, M. Eliáš, and L. Zajíčková, Phys. Status Solidi A **211**, 2801 (2014).
[27]A. Manakhov, D. Nečas, J. Čechal, D. Pavliňák, M. Eliáš, and L. Zajíčková, Thin Solid Films **581**, 7 (2015).
[28]A. Manakhov, E. Makhneva, P. Skládal, D. Nečas, J. Čechal, L. Kalina, M. Eliáš, and L. Zajíčková, Appl. Surf. Sci. **360**, 28 (2016).
[29]E. Makhneva, A. Manakhov, P. Skládal, and L. Zajíčková, Surf. Coat. Technol. **290**, 116 (2016).
[30]L. Štrbková, A. Manakhov, L. Zajíčková, A. Stoica, P. Veselý, and R. Chmelík, Surf. Coat. Technol. **295**, 70 (2016).
[31]A. Manakhov, M. Landová, J. Medalová, M. Michlíček, J. Polčák, D. Nečas, and L. Zajíčková, Plasma Process. Polym. **14**, 1600123 (2017).
[32]C. Vandenabeele, M. Buddhadasa, P.-L. Girard-Lauriault, and R. Snyders, Thin Solid Films **630**, 100 (2017).
[33]M. Buddhadasa, C. R. Vandenabeele, R. Snyders, and P.-L. Girard-Lauriault, Plasma Process. Polym. **14**, 1700030 (2017).
[34]W. Z. Collison, T. Q. Ni, and M. S. Barnes, J. Vac. Sci. Technol. A **16**, 100 (1998).
[35]C. S. Corr, E. Despiau-Pujo, P. Chabert, W. G. Graham, F. G. Marro, and D. B. Graves, J. Phys. D Appl. Phys. **41**, 185202 (2008).
[36]A. Hurlbatt, A. R. Gibson, S. Schröter, J. Bredin, A. P. S. Foote, P. Grondein, D. O'Connell, and T. Gans, Plasma Process. Polym. **14**, 1600138 (2017).
[37]A. Bogaerts, E. Bultinck, M. Eckert, V. Georgieva, M. Mao, E. Neyts, and L. Schwaederlé, Plasma Process. Polym. **6**, 295 (2009).
[38]S. Stoykov, C. Eggs, and U. Kortshagen, J. Phys. D Appl. Phys. **34**, 2160 (2001).
[39]M. Mao, J. Benedikt, A. Consoli, and A. Bogaerts, J. Phys. D Appl. Phys. **41**, 225201 (2008).
[40]Y. Miyagawa, H. Nakadate, M. Tanaka, M. Ikeyama, S. Nakao, and S. Miyagawa, Surf. Coat. Technol. **201**, 8414 (2007).
[41]D. A. Ariskin, I. V. Schweigert, A. L. Alexandrov, A. Bogaerts, and F. M. Peeters, J. Appl. Phys. **105**, 063305 (2009).
[42]K. Ostrikov, H.-J. Yoon, A. E. Rider, and S. V. Vladimirov, Plasma Process. Polym. **4**, 27 (2007).
[43]V. N. Volynets, A. V. Lukyanova, A. T. Rakhimov, D. I. Slovetsky, and N. V. Suetin, J. Phys. D Appl. Phys. **26**, 647 (1993).
[44]E. Gogolides, M. Stathakopoulos, and A. Boudouvis, J. Phys. D Appl. Phys. **27**, 1878 (1994).
[45]Y.-R. Zhang, S. Tinck, P. D. Schepper, Y.-N. Wang, and A. Bogaerts, J. Vac. Sci. Technol. A **33**, 021310 (2015).
[46]A. L. Alexandrov and I. V. Schweigert, Plasma Sources Sci. Technol. **14**, 209 (2005).
[47]H. C. Thejaswini, S. Peglow, U. Martens, V. Sushkov, and R. Hippler, Contrib. Plasma Phys. **54**, 683 (2014).
[48]S.-X. Zhao, Y.-R. Zhang, F. Gao, Y.-N. Wang, and A. Bogaerts, J. Appl. Phys. **117**, 243303 (2015).
[49]H. C. Kim, F. Iza, S. S. Yang, M. Radmilović-Radjenović, and J. K. Lee, J. Phys. D Appl. Phys. **38**, R283 (2005).
[50]D. J. Economou, Plasma Process. Polym. **14**, 1600152 (2017).
[51]C. K. Birdsall and A. B. Langdon, *Plasma Physics Via Computer Simulation* (Taylor & Francis, London, 2005).
[52]D. Tskhakaya, K. Matyash, R. Schneider, and F. Taccogna, Contrib. Plasma Phys. **47**, 563 (2007).
[53]G. A. Bird, *Molecular Gas Dynamics and the Direct Simulation of Gas Flows* (Clarendon, Oxford, 1994).

Published under license by AVS.

[54]C. Schwanke, A. Pflug, M. Siemers, and B. Szyszka, "Parallel particle-in-cell Monte-Carlo algorithm for simulation of gas discharges under PVM and MPI," in *Lecture Notes in Computer Science*, edited by K. Jónasson (Springer, Berlin, 2010), Vol. 7133, p. 213.
[55]S. Mathioudaki, C. Vandenabeele, R. Tonneau, A. Pflug, and S. Lucas, J. Vac. Sci. Technol. A **37**, 031301 (2019).
[56]J. Tennyson, Phys. Rep. **491**, 29 (2010).
[57]C. R. Vandenabeele and S. Lucas, Mater. Sci. Eng. R **139**, 100521 (2020).
[58]D. Graham, Spectragui, NESAC/BIO, 2014, https://www.nb.uw.edu/mvsa/spectragui.
[59]J. E. Jackson, *A User's Guide to Principal Components* (Wiley, New York, 2005).
[60]D. J. Graham and B. D. Ratner, Langmuir **18**, 5861 (2002).
[61]C. Jeynes, N. P. Barradas, P. K. Marriott, G. Boudreault, M. Jenkin, E. Wendler, and R. P. Webb, J. Phys. D Appl. Phys. **36**, R97 (2003).
[62]A. F. Gurbich, Nucl. Instrum. Methods Phys. Res. B **371**, 27 (2016).
[63]Y.-K. Kim and M. E. Rudd, Phys. Rev. A **50**, 3954 (1994).
[64]N. F. Mott and R. H. Fowler, Proc. R. Soc. Lond. Ser. A **126**, 259 (1930).
[65]H. Bethe, Ann. Phys. **397**, 325 (1930).
[66]H.-J. Werner, P. J. Knowles, G. Knizia, F. R. Manby, and M. Schütz, Wiley Interdiscip. Rev. Comput. Mol. Sci. **2**, 242 (2012).
[67]M.-Y. Song, J.-S. Yoon, H. Cho, Y. Itikawa, G. P. Karwasz, V. Kokoouline, Y. Nakamura, and J. Tennyson, J. Phys. Chem. Ref. Data **44**, 023101 (2015).
[68]M.-Y. Song, J.-S. Yoon, H. Cho, G. P. Karwasz, V. Kokoouline, Y. Nakamura, and J. Tennyson, J. Phys. Chem. Ref. Data **46**, 013106 (2017).
[69]D. D. Wagman, W. H. Evans, V. B. Parker, I. Halow, S. M. Bailey, and R. H. Schumm, *Selected Values of Chemical Thermodynamic Properties. Tables for the First Thirty-Four Elements in the Standard Order of Arrangement* (Institute for Basic Standards, National Bureau of Standards, Washington, DC, 1968).
[70]D. D. Wagman, W. H. Evans, V. B. Parker, I. Halow, S. M. Bailey, and R. H. Schumm, *Selected Values of Chemical Thermodynamic Properties. Tables for Elements 35-53 in the Standard Order of Arrangement* (Institute for Basic Standards, National Bureau of Standards, Washington, DC, 1969).
[71]V. H. Dibeler and S. K. Liston, J. Chem. Phys. **48**, 4765 (1968).
[72]R. F. Pottie and F. P. Lossing, J. Am. Chem. Soc. **85**, 269 (1963).
[73]J. A. Kerr, Chem. Rev. **66**, 465 (1966).
[74]Y.-R. Luo, "Bond dissociation energies," in *CRC Handbook of Chemistry and Physics*, 89th ed., edited by D. R. Lide (CRC/Taylor and Francis, Boca Raton, FL, 2009).
[75]W. D. Good and R. T. Moore, J. Chem. Thermodyn. **3**, 701 (1971).
[76]T. L. Cottrell, *The Strength of Chemical Bonds* (Butterworths, London, 1954).
[77]S. W. Benson, J. Chem. Educ. **42**, 502 (1965).
[78]L. Brewer, W. T. Hicks, and O. H. Krikorian, J. Chem. Phys. **36**, 182 (1962).
[79]V. I. Vedeneev, *Bond Energies, Ionization Potentials and Electron Affinities* (St. Martin's, New York, 1966), 202 p.
[80]J. R. Hamilton, J. Tennyson, S. Huang, and M. J. Kushner, Plasma Sources Sci. Technol. **26**, 065010 (2017).
[81]P. G. Burke, *R-Matrix Theory of Atomic Collisions: Application to Atomic, Molecular and Optical Processes* (Springer, Berlin, 2011).
[82]J. M. Carr *et al.*, Eur. Phys. J. D **66**, 58 (2012).
[83]J. Tennyson, D. B. Brown, J. J. Munro, I. Rozum, H. N. Varambhia, and N. Vinci, J. Phys. Conf. Ser. **86**, 012001 (2007).
[84]W. J. Brigg, J. Tennyson, and M. Plummer, J. Phys. B At. Mol. Opt. Phys. **47**, 185203 (2014).
[85]N. Sanna and F. A. Gianturco, Comput. Phys. Commun. **114**, 142 (1998).
[86]R. D. Johnson III, "NIST Computational Chemistry Comparison and Benchmark DataBase," NIST Standard Reference Database Number 101 (National Institute of Standards and Technology, Gaithersburg, MD, 2018), see http://cccbdb.nist.gov/.
[87]D. K. Hendricksen and M. D. Harmony, J. Chem. Phys. **51**, 700 (1969).
[88]A. Faure and J. Tennyson, Mon. Not. R. Astron. Soc. **325**, 443 (2001).
[89]A. Pflug, M. Siemers, C. Schwanke, B. Febty Kurnia, V. Sittinger, and B. Szyszka, Mater. Technol. **26**, 10 (2011).
[90]A. Pflug, M. Siemers, T. Melzig, L. Schäfer, and G. Bräuer, Surf. Coat. Technol. **260**, 411 (2014).
[91]A. Pflug, M. Siemers, T. Melzig, D. Rademacher, T. Zickenrott, and M. Vergöhl, Surf. Coat. Technol. **241**, 45 (2014).
[92]A. Pflug, M. Höfer, T. Harig, M. Armgardt, C. Britze, M. Siemers, T. Melzig, and L. Schäfer, Thin Solid Films **595**, 266 (2015).
[93]C. Geuzaine and J.-F. Remacle, Int. J. Numer. Methods Eng. **79**, 1309 (2009).
[94]C. A. Brebbia and R. Magureanu, Eng. Anal. **4**, 178 (1987).
[95]K. Koura and H. Matsumoto, Phys. Fluids A **3**, 2459 (1991).
[96]C. Vandenabeele, R. Maurau, S. Bulou, F. Siffer, M. Gérard, T. Belmonte, and P. Choquet, Plasma Process. Polym. **11**, 1089 (2014).
[97]M. E. Moustapha, J. F. Friedrich, Z. R. Farag, S. Krüger, G. Hidde, and M. M. Azzam, "Promotion of adhesion of green flame retardant coatings onto polyolefins by depositing ultra-thin plasma polymer films," in *Progress in Adhesion and Adhesives*, edited by K. Mittal (Wiley, Hoboken, NJ, 2017), p. 399.
[98]S. Zhang, X. Lam Bui, X. T. Zeng, and X. Li, Thin Solid Films **482**, 138 (2005).
[99]R. F. Bunshah, *Handbook of Deposition Technologies for Films and Coatings: Science, Technology, and Applications* (Noyes, Park Ridge, NJ, 1994).
[100]M. Ohring, *Materials Science of Thin Films* (Elsevier Science, New York, 2001).
[101]A. V. Naumkin, A. Kraut-Vas, S. W. Gaarenstroom, and C. J. Powell, "NIST X-ray Photoelectron Spectroscopy Database," Version 4.1 (National Institute of Standards and Technology, Gaithersburg, MD, 2012), see https://srdata.nist.gov/xps/.
[102]A. Nelson, B. W. Muir, J. Oldham, C. Fong, K. M. McLean, P. G. Hartley, S. K. Øiseth, and M. James, Langmuir **22**, 453 (2006).
[103]C. Hopf, T. Schwarz-Selinger, W. Jacob, and A. V. Keudell, J. Appl. Phys. **87**, 2719 (2000).
[104]J. Ryssy, E. Prioste-Amaral, D. F. N. Assuncao, N. Rogers, G. T. S. Kirby, L. E. Smith, and A. Michelmore, Phys. Chem. Chem. Phys. **18**, 4496 (2016).
[105]G. Ertl, Surf. Sci. **299–300**, 742 (1994).
[106]W. H. Weinberg, Acc. Chem. Res. **29**, 479 (1996).

Published under license by AVS.